Integrating a double cropping model with groundwater-fed irrigation in the North China Plain

Yuwen Fan[1], Zhao Yang[2], Min-Hui Lo[3] and Eun-Soon Im[1,4]

[1] Division of Environment and Sustainability, The Hong Kong University of Science and Technology, Hong Kong, China

[2] Pacific Northwest National Laboratory, Richland, WA, USA

[3] Department of Atmospheric Sciences, National Taiwan University, Taipei, Taiwan

[4] Department of Civil and Environmental Engineering, The Hong Kong University of Science and Technology, Hong Kong, China

Corresponding author: Yuwen Fan (yfanaj@connect.ust.hk), Eun-Soon Im (ceim@ust.hk)

Key Points:

- The implementation of the widely adopted double cropping rotation allows for a significantly improved simulation of crop phenology in NCP.
- The water-sensitive crop simulation underscores the importance of irrigation in maintaining compact rotation and high productivity in NCP.
- The use of province-based thresholds and crop-followed applications effectively captures the spatial variability of irrigation consumption.

Abstract

Irrigated cultivation, as a prevalent anthropogenic activity, exerts a significant influence on land use and land cover, resulting in notable modifications to land-atmosphere interaction and the hydrological cycle. Given the extensive cropland, high productivity, compact rotation, semi-arid climate, intense irrigation, and groundwater depletion in the North China Plain (NCP), the development of a comprehensive crop-irrigation-groundwater model becomes imperative for understanding agricultural-induced climate response in this region. This study presents an integrated crop model explicitly tailored to the NCP, which incorporates double-cropping rotation, irrigation practice, and groundwater interactions into the regional climate model. The modifications are implemented to: (1) enable a seamless transition from field scale application to regional scale application, facilitating the incorporation of spatial variability, (2) capture the distinctive attributes of the NCP region, ensuring the model accurately reflects its unique characteristics, and (3) reinforce the direct interaction among crop-related variables, thereby enhancing the model's capacity to simulate their dynamic behaviors. The integrated crop modeling system demonstrates a commendable performance in crop simulations using climatic conditions, which is substantiated by its identification of crop stages, estimation of field biomass, prediction of crop yield, and finally the projection of monthly leaf area index. In our next phase, this integrated crop modeling system will be employed in long-term simulations to enhance our understanding of the intricate relationship between agricultural development and climate change.

Plain Language Summary

Irrigated cropping in the North China Plain (NCP) have a significant impact on the regional climate and water cycle. To better understand how agriculture affects the climate in this region, we developed a comprehensive crop-irrigation-groundwater model. This model specifically focuses on the NCP region and includes double-cropping rotation, irrigation practices, and groundwater dynamics. By comparing with the observation, the integrated model make great improvement in simulating crop stages, leaf and stem mass, crop yield, and vegetation greeness. In the next phase, we will use this model to study the long-term effects of agricultural development on climate change in the NCP.

1 Introduction

Agriculture is one of the primary drivers of land use changes (Goldewijk, 2001) and the largest consumer of water resources globally (Foley et al., 2011). To increase crop productivity and feed the exploding population, irrigation has rapidly expanded in the past decades, and accounts for over 70% of the global freshwater withdrawal today, exerting a significant influence on the hydroclimate (McDermid et al., 2023; S. Siebert et al., 2010). As surface water becomes increasingly scarce, groundwater is then being exploited to meet the demands of intensive irrigation, particularly in semi-arid regions or during the dry season (Famiglietti, 2014; Wada et al., 2012). The overexploitation of groundwater resources can lead to depletion of soil moisture and freshwater availability, as well as potential disasters such as land subsidence and seawater intrusion (An et al., 2021; Famiglietti, 2014). While cultivation practices gradually alter the climatic processes, it is also worth noting that the changing climate also influences back onto crop production (Ahmed et al., 2015; M. Yang & Wang, 2023). Hence, it is imperative to incorporate the cultivation-climate interactions into the current climate models, specifically into the land-surface models (LSMs), to better simulate and understand the complex relationships between agriculture and climate change.

Although agriculture has not been explicitly represented in most regional climate models (Oleson et al., 2013), few relevant schemes are already implemented. Several crop models have been designed to capture the seasonal and interannual pattern of crop phenology, such as leaf area index and biomass (X. Liu et al., 2016; Oleson et al., 2013; Yin & van Laar, 2005). Unlike generic dynamic vegetation schemes, these crop models can identify current crop stages (e.g., emergence, reproduction) based on the climate conditions (e.g., temperature, sunshine), calculate vegetation growth in different crop stages (e.g., growth rate, carbon allocation), as well as simulate the human practices (e.g., planting and harvesting). Furthermore, irrigation can be applied with a fixed amount (Vira et al., 2019) or dynamically based on soil conditions (Ozdogan et al., 2010; Qian et al., 2013; Valayamkunnath et al., 2021; L. Wu et al., 2018; B. Yang et al., 2016; Z. Yang et al., 2017, 2019, 2020), which has improved the understanding of the climate response to irrigation. Although it has been generally agreed that irrigation has a cooling and moistening effect globally (Cook et al., 2011; Lo et al., 2021; Pokhrel et al., 2012; Puma & Cook, 2010), its influence is non-linear and location-specific at regional scales, as it greatly depends on the agricultural and climatic conditions of the region in which it is deployed (Yuwen Fan et al., 2023; Im et al., 2014; Kang & Eltahir, 2018, 2019; Pei et al., 2016; Tuinenburg et al., 2014; Wey et al., 2015; Z. Yang et al., 2019). Independent with the crop modules and irrigation schemes, some groundwater models parameterize the soil-groundwater interactions such as downward drainage and capillary rise (Lo & Famiglietti, 2011; Niu et al., 2007, 2011). In addition to vertical water transportation, lateral flow (Ying Fan et al., 2007; Kabir et al., 2023; Miguez-Macho et al., 2007; Zeng et al., 2018) and human consumption (Anderson et al., 2015; Kabir et al., 2023; L. Wang et al., 2020) have also been included in the subsurface process to complete the groundwater dynamics. The implementation of the groundwater sector shows its potential to reduce dry and hot biases over the central United States, as groundwater replenishes the nearby river and root-zone soils (L. Wang et al., 2020).

Prior research has demonstrated a widespread potential for simulating cultivation including crop phenology, irrigation practices, and groundwater storage. Additionally, these modules have been integrated to address more complex processes. A common approach is to combine a crop module with irrigation activity (Xu et al., 2019; B. Yang et al., 2016; Z. Zhang et al., 2020), which has resulted in significant enhancements in crop yield predictions and a better understanding of irrigation impact. Other studies have joint soil-moisture-dependent irrigation with the unconfined layer (Kabir et al., 2023; Leng et al., 2014; L. Wu et al., 2018), improving model performance in reproducing the latent heat and soil moisture (Wang 2020). However, few studies comprehensively considered all of these factors simultaneously, especially in regional climate models. Given the close and complex relationships between these processes, any missing component would lead to inadequacies in representing the climatic process over croplands. Therefore, there is an increasing need to develop a joint crop-irrigation-groundwater model in LSMs.

As a key agricultural region, the North China Plain (NCP) encompasses more than 40% of China's total harvested area (FAO, 2019). Approximately two-thirds of the land within the NCP is dedicated to cropland, contributing to nearly half of the national wheat production and one-third of the corn production (E. Wang et al., 2008). The significance of NCP for agricultural study is rooted not only in its extensive cropland and high productivity, but also in its compact rotation, semi-arid background, intense irrigation, and groundwater depletion, which makes the NCP an ideal testbed for evaluating the integrated crop modeling system. To maintain its high productivity, a double-cropping system, typically winter wheat with summer maize, is widely adopted in NCP (Jiang et al., 2021). However, the annual precipitation in NCP is only around 800mm, which is almost half of that in southern China (Zhe et al., 2014), increasing its dependency on irrigation, especially from groundwater. About 40% of the farmland on the NCP is reliant on irrigation (Portmann et al., 2010; Stefan Siebert et al., 2013), with around 62% of the water usage coming from underground (J. Wang et al., 2019). The relatively dry climate in the NCP makes it more sensitive to the additional water induced by the intense irrigation (Yuwen Fan et al., 2023), and groundwater overexploitation has led to a rapid expansion of above-ground water storage, potentially causing long-term hydrological alterations (Y. Zhou et al., 2022). All of these imply that the crop modelling system for the NCP region needs to consider all the interactions between crop growth, irrigation practice, and groundwater usage, which will have further implications for the long-term agriculture and climate in the region.

Given the unique characteristics of the NCP, our research aims to develop an integrated crop model with irrigation and groundwater interaction, specifically tailored for the NCP and its surrounding region. In light of the reasonable performance of various related schemes, the main focus of this study is to combine these components together with appropriate modifications, instead of reinventing new algorithms. To achieve this, Noah-Multiparameterization (Noah-MP) has been selected, as it already encompasses several functions related to cultivation simulation. It is conducted online with the Weather Research Forecast (WRF) to include the two-way nested feedback between the crop system and climate dynamics. Moreover, regionalization becomes imperative since certain schemes within Noah-MP are primarily developed and calibrated based on local field observations in the United States. Although the

general algorithm might be applicable worldwide, the specific details or parameters may not be suitable for the NCP. For instance, it is necessary to consider the prevailing practice of double cropping rotation since it has the potential to greatly affect the vegetation pattern and irrigation demand. Also, applying spatially varied crop calendars and irrigation thresholds according to the regional-specific observation, rather than a uniform value, can greatly improve crop yields and irrigation amount (Xu et al., 2019; Z. Zhang et al., 2020). And large regional uncertainties may exist in some parameters such as leaf area per living leaf biomass (BIO2LAI, also known as specific leaf area) (Yu et al., 2022; Z. Zhang et al., 2020). Hence, we conduct parameter calibration and adopt local inputs. While regionalizing the model, the generality should also be considered to ensure its potential application in other regions or other climate models. By integrating and regionalizing the crop modelling system, this study primarily focuses on the model development and its predictability assessment in crop phenology and irrigation requirements. However, there is a great potential for applying it in long-term simulation, which represents a promising avenue for advancing our understanding of the coupled human-natural system.

2 Model Description and Experiment Design

The study domain is centered on the NCP, encompassing a significant portion of China's cropland. Considering the specific attributes of the study area, modifications are made under the following conditions: (1) to facilitate the transition from field scale application to regional scale application, enabling the incorporation of spatial variability, (2) to capture the local specialties of the NCP region, ensuring the model accurately represents its unique characteristics, (3) to complement the direct interaction among crop-related variables, enhancing the model's ability to simulate their dynamics. Experiments are designed to compare the model's performance with and without these modifications.

2.1 Study Area

Figure 1 illustrates some key background variables, outlining the NCP region within black boxes. The topography and cropland fraction are basic geostatic inputs for the WRF, initially retrieved from the United States Geological Survey and Moderate-resolution Imaging Spectroradiometer (MODIS), respectively. Notably, the NCP region, being the largest plain in eastern China, exhibits an average elevation even below 100m (Figure 1b), contributing to its suitability for cultivation. Despite the high cropland fraction exceeding 95% in most of the pluvial area (Figure 1c), the climatology annual precipitation (retrieved from China Meteorological Forcing Dataset) in 2000-2009 is merely half that of southern China (Figure 1a), highlighting the need for irrigation. According to the FAO AQUASTAT database (Stefan Siebert et al., 2013), irrigated cropland constituted more than 70% of the total land use in the pluvial area in 2005 (Figure 1d). Given the scarcity of surface water in northern China, groundwater plays a crucial role in meeting the substantial irrigation demand (Figure 1e).

Statistical data indicates that groundwater dependence in Hebei and Henan provinces reached 70% and 60%, respectively (National Bureau of Statistics of China, 2005).

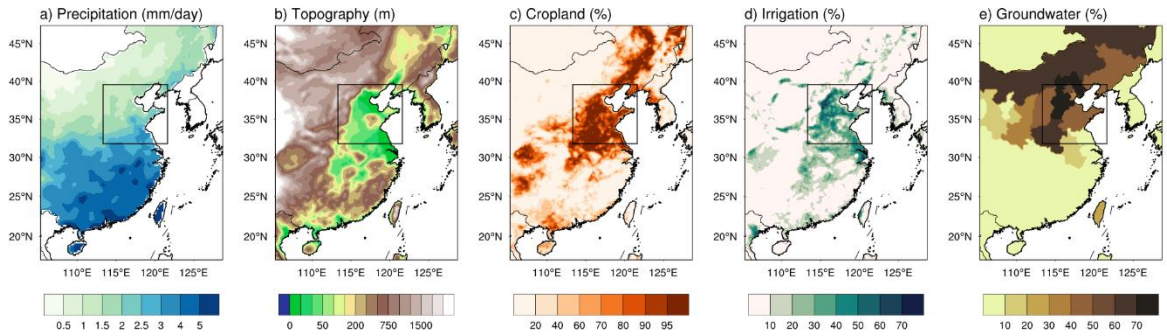

Figure 1. (a) Annual precipitation (mm/day) and basic geostatic variables applied in this project including (b) topography (m), (c) cropland fraction (%), (d) irrigated land fraction (%), (e) groundwater dependence (%).

2.2 Model Configuration and Experiment Design

The study employs the Advanced Research version of the WRF Model (version 4.3), a non-hydrostatic numerical weather prediction model that has been widely adopted in regional studies. The horizontal grid spacing is 27km, with 38 vertical layers in the atmosphere and 4 soil layers below the ground. Its physical options mostly follows Fan et al. (2023), including the WRF double-moment 5-class microphysical parameterization (Hong et al., 2004), the Rapid Radiative Transfer Model as the longwave radiation scheme (Mlawer et al., 1997), the Dudhia shortwave radiation scheme (Dudhia, 1989), the Yonsei University planetary boundary layer scheme (Hong et al., 2006), the scale-aware New Simplified Arakawa-Schubert scheme (Han & Pan, 2011; Kwon & Hong, 2017), and Noah-MP land surface model coupled with our improved crop, irrigation and groundwater schemes (Ek et al., 2003). The initial and lateral boundary conditions are obtained from the ERA5 reanalysis dataset, with 6-hour output intervals, which helps to reduce the uncertainty arising from the boundary condition (Hersbach et al., 2020).

Table 1. Description of all experiments

Experiment	Model		
	Crop	Irrigation	Groundwater
CTL			
CROPdef	default version		
CROPnew	improved version		
IRRdef	improved version	default version	
IRRnew	improved version	improved version	
GWnew	improved version	improved version	improved version

We conduct multiple experiments to validate the crop growth and irrigation behaviour in 2005, which has a normal value of the East Asian Summer Monsoon Index. Considering that winter wheat is typically sown in the autumn of the preceding year, all experiments are started on 1 March 2004. This allows for a spinning-up period of at least six months prior to the 2004-2005 crop season, ensuring that the model was appropriately initialized for accurate simulations. When examining the intra-annual pattern (e.g., monthly crop growth), we only present the monthly pattern specifically in the year 2005.

Detailed information regarding all experiments can be found in Table 1, including the choices of crop, irrigation, and groundwater models. All models are inactive in the control experiment (CTL), in which static vegetation with predefined monthly patterns from satellite data is employed. The crop and irrigation model can be applied either in the default version or the improved version. The default crop model is conducted using the original scheme proposed by Liu et al. (2016) and parameters derived from Zhang et al. (2020), while the improved crop model involves both modifications to the algorithms and recalibration of the parameters. In order to exclusively demonstrate the advancements made by the crop model, the irrigation component remains inactive in both CROPdef and CROPnew. This implies that no supplementary water is introduced to the cropland, thereby highlighting the impact solely attributed to the enhancements made within the crop model. The added value of our improvements on the irrigation model can be discerned through a straightforward comparison between IRRdef and IRRnew experiments. In IRRdef, the default version of dynamic irrigation is derived from He et al. (2023) and serves as the baseline for the improved version. In the default version, the target soil moisture availability as a parameter threshold is uniformly set to 0.8, as suggested by Fan et al. (2023), while in the improved version, it exhibits spatial variability between provinces. Finally in GWnew, we incorporate the irrigation extraction process into Miguez-Macho et al. (2007) groundwater scheme, together with the improved crop and irrigation model, to visualize the distinct effects on crop prediction resulting from the interactions between groundwater and soil. The detailed improvements made to the crop, irrigation, and groundwater models will be explained in Sections 2.3, 2.4, and 2.5, respectively.

2.3. Modification of the crop model

2.3.1 Crop area and FVEG prediction

In order to achieve efficient computation, the crop module developed by Liu et al. (2016) is selected as the foundation for crop simulation. This module operates based on the planting and harvesting dates, using growing degree days (GDD) to predict the growth stages on a yearly routine. The growth rate and carbohydrate accumulation are primarily influenced by factors such as photosynthesis and respiration, which are sensitive to crop mass, water stress, soil temperature, CO_2 concentration, and solar radiation. Then, these carbohydrates are allocated among different plant components, including leaves, stems, roots, and grains, dedicated by distribution schemes that vary with the growth stage. This particular crop model was initially designed for crop fields and thus applied uniformly to all the grids within the domain. However, to extend its application to a larger domain that has various land-use types, the model needs to be exclusively activated on crop grids, while non-crop grids utilize prescribed vegetation. A

crop grid is defined based on MODIS land-use classification as either 'Croplands' or 'Cropland/Natural Vegetation Mosaic'. This definition aligns with Fan et al. (2023), and is similar to the approach employed by Yu et al. (2022) who set a threshold of 50% cropland percentage, since the majority of grids in the NCP region contain over 90% cropland (Figure 1c).

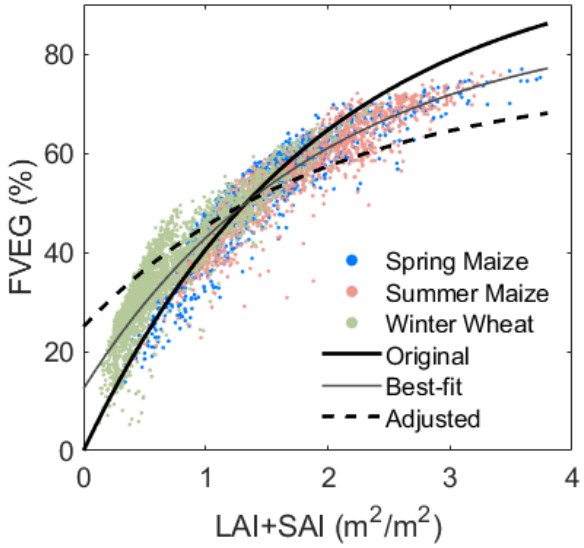

Figure 2. The relationship between FVEG and LAI+SAI in the NCP region. The thick solid line presents the original empirical relationship (Equation 1), the fine solid line for the best-fit relationship, and while thick dash line for the adjusted equation (Equation 2).

Although the dynamic leaf area index (LAI) and stem area index (SAI) can be calculated based on crop growth and climate conditions, the default crop model sets the vegetation fraction (FVEG) to the maximum value (i.e., 95%) for all grids, to represent the dense vegetation in the crop field. However, this fixed value might not be appropriate for regional-scale applications. Considering the long-term impact of FVEG variability through vegetative radiation and canopy interception (W. Liu et al., 2020; D. Wang et al., 2007), we correlate FVEG with the LAI/SAI using the empirical relationships (Equation 1) proposed by Niu et al. (2011) and further testified by Wu et al. (2018) in the NCP region. However, according to the MODIS observation retrieved from the input of the CTL, it is imperative to note that the original curve underestimates the FVEG at low LAI+SAI and overestimates it at high LAI+SAI (Figure 2), which poses a potential risk to the reliability of the predictions. More specifically, at the onset of the crop season, accurate LAI+SAI estimation leads to an underestimation of the calculated FVEG. This, in turn, results in reduced shortwave radiation intercepted by vegetation and a slower rate of photosynthesis. Consequently, the leaf growth is undervalued in the next timestep, and the less LAI creates a larger bias on the FVEG prediction. This positive feedback continues to accumulate underestimation during subsequent iterations, and ultimately, results in the failure of the entire crop season. Similarly, the curve exhibits an exaggerated FVEG during the flourishing period, which easily leads to uncontrollable overgrowth. This susceptibility underscores the necessity to consider and address this inherent limitation. Even when employing the best-fitting curve, this issue persists for almost half of the grids. Therefore, we propose a constraint on the range of FVEG, limiting it to [0.25, 0.75], instead of utilizing the full range of [0, 1]. This allows for a slight overestimation in the initial stages and an

underestimation towards the end, ensuring a successful startup and a steady progression toward its peak. The adjustment on this equation enables the spatial and temporal variations of FVEG, as well as the vegetation responses to the irrigation application.

$$\text{Original FVEG} = 1 - e^{(-0.52\times(\text{LAI}+\text{SAI}))}, \text{FVEG} \in [0,1] \quad (1)$$

$$\text{Adjusted FVEG} = 0.75 - 0.5 \times e^{(-0.52\times(\text{LAI}+\text{SAI}))}, \text{FVEG} \in [0.25,0.75] \quad (2)$$

2.3.2 From single cropping to double cropping

The default model only considers single cropping, allowing one crop type per grid but different crops spatially. However, NCP widely adopts double-cropping rotation, as evident from satellite vegetation patterns (Qiu et al., 2022; W. Wu et al., 2010; Yan et al., 2014; Yuan et al., 2020). The first growing season typically begins in late spring to early summer and extends until mid to late autumn, followed immediately by the second growing season which stops just before the restart of the first growing season. And it's necessary to consider the second crop season in the crop-irrigation-groundwater system, because the dry soil in the winter and spring probably requires significant irrigation and groundwater supply (Yuwen Fan et al., 2023; Koch et al., 2020; L. Wu et al., 2018; B. Yang et al., 2016). According to the prevalence (Qiu et al., 2022; W. Wu et al., 2010), we select winter wheat and summer maize for double cropping region (shown in orange in Figure 3a), as identified by satellite data (Qiu et al., 2022), and spring maize for single cropping region (shown in blue in Figure 3a).

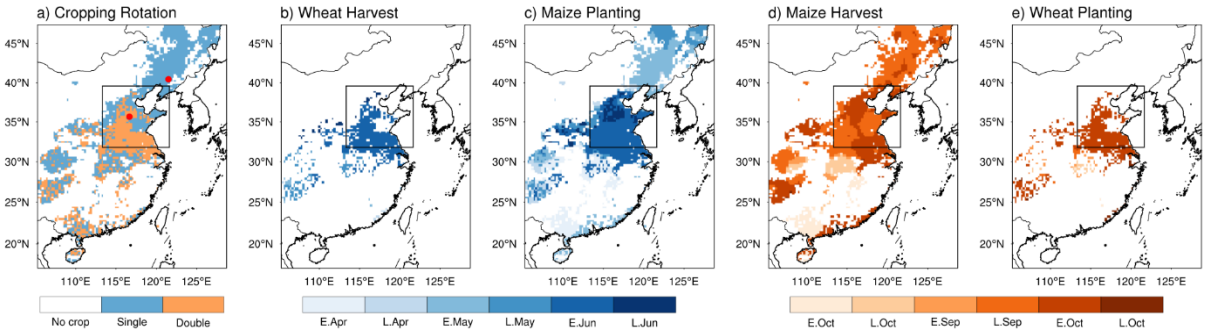

Figure 3. Spatial distribution of (a) the cropping system, (b-e) harvest date and planting date for wheat and maize over a year based on the chronological order.

The planting date and the harvesting date are fed into the crop model as the definition of the crop seasons, whose spatial variability is claimed to be beneficial to the accuracy of crop growth prediction (Xu et al., 2019; Z. Zhang et al., 2020). The harvesting date of the spring maize is assigned to be 15 days after the physiological maturity date obtained from a satellite-based post-processed dataset (Luo et al., 2020). The planting date is determined as 15 days prior to the V3 stage, which represents the early vegetative stage of maize when the third leaf is fully expanded. Similarly, for double-cropping regions, the maturity dates of wheat and maize, with a 15-day buffer, mark the end of the respective cropping seasons, while the

subsequent cropping season starts 5 days later. The ’15-day’ buffer and ‘5-day’ interval are roughly defined according to the LAI pattern in Luo et al. (2020). Few grids not covered by the satellite dataset are assigned 1 May (121st Julian Day) and 11 October (284th Julian Day) as the default planting and harvesting date for maize, respectively, based on field study (Yu et al., 2022). The planting date and the harvesting date also perform similar spatial patterns to those generated by Wu et al. (2010).

2.3.3 Input Setting and Parameter Calibration

We begin with the parameters for one-year corn in Bondville (Z. Zhang et al., 2020), and calibrate them using data from two ChinaFlux sites, Yucheng (36.83°N, 116.57°E) for double-cropping and Shenyang (41.52°N, 123.39°E) which is nearby the NCP region for single-cropping, as indicated in Figure 2a. In the case of spring maize and summer maize, we first try to adopt the parameters from previous studies and recalibrate if necessary, to keep the generality. Conversely, a new set of parameters is developed specifically for winter wheat, drawing upon statistical information from the Yucheng station, satellite datasets, and other agronomy studies (Y. Zhang et al., 1991; Z. Zhang et al., 2023). Table S1 provides the adjusted parameters for wheat and maize, along with the supporting scientific references. The recalibration sequences are as follows.

The recalibration starts from crop-stage identification, since it relies purely on the accumulated Growing Degrees Days (GDD) and is less affected by other crop parameters. The GDD-related parameters are retrieved from Zhang et al. (2020) and Zhang et al. (1991), and then validated with the heading date and maturity date retrieved from the satellite data (Luo et al., 2020). The crop stage comprises the pre-planting stage, three vegetative stages (emergence, initial vegetative, post-vegetative), two reproductive stages (initial reproductive, post-reproductive), and finally, one maturity stage. During the vegetative stage, a majority of carbohydrates are allocated to the leaves and stems, while in the reproductive stage, the allocation shifts towards the grain. In our simulation results, we consider the transition date from post vegetative stage to the initial reproductive stage as the heading date. This allows us to capture the transfer of focus from leaf development to grain formation, aligning it with the time of maximum Leaf Area Index (LAI) identified by the satellite and facilitating meaningful comparisons.

Next, the general growth rate including BIO2LAI can be extracted from the station data, and the Maximum rate of carboxylation at 25 °C (VCMX25) can also be estimated using the monthly satellite data of Gross Primary Product (GPP) and LAI, since the photosynthesis rate and the LAI are approximately linearly related, especially on sunny days when the canopy temperature is around 25°C (He et al., 2023). Instead of the linearly interpolated data from WRF pre-processing, both GPP and LAI that we adopted are initially derived from MODIS products but have undergone further post-processing to generate a more continuous monthly pattern (S. Wang et al., 2020; Yuan et al., 2020), and will be considered as the observation (OBS). Furthermore, the AVCMX, which represents the crop sensitivity to the temperature, can be determined by the gradient of biomass accumulation (H. Huang et al., 2022), especially in spring and autumn with greater temperature changes. For maize, the values of VCMX25 and

AVCMX have simply followed the previous studies, while BIO2LAI is subject to recalibration, as its necessity of recalibration has been demonstrated by Yu et al. (2022).

Following the establishment of the general photosynthesis rate, we proceed to fine-tune the distribution of carbohydrates among the leaf, stem, and grain compartments, based on the annual cycle of leaf mass and stem data obtained from the station data. Any remaining carbohydrates are allocated to the root. In cases where the recalibration of the distribution scheme alone does not yield satisfactory predictions, adjustments to the turnover and translocation rates are implemented. Additionally, the crop yield will be validated through comparisons with remotely sensed estimations from Cheng et al. (2022).

Finally, the incorporation of irrigation and groundwater modules into the crop model may introduce deviations in crop growth and affect the predictability of associated parameters. As a result, slight adjustments are made after the integration. In essence, the crop-irrigation-groundwater system, conducted in GWnew, aims to provide the most accurate simulation since it reflects the closest approximation to reality.

2.4 Modification of the irrigation model

In this study focusing on the NCP, which predominantly practices dryland cultivation, the irrigation methods will mostly pertain to dryland irrigation, excluding grassland irrigation and paddy field irrigation. To avoid difficulties in modeling canopy interception and surface losses inherent in sprinkler and fast flooding techniques, we opt for drip irrigation using the Noah-MP version 5.0 model (He et al., 2023). This choice simplifies the system while maximizing water resource utilization. The default irrigation module is employed from the planting date to the harvesting date. In order to establish a stronger connection between irrigation and crop growth, irrigation is initiated upon crop emergence and discontinued upon physiological maturity. Thus, a reciprocal relationship between crop growth and irrigation is established. The cooling effect resulting from irrigation extends the crop season, and in turn, requires a longer irrigation period.

The default irrigation is activated all day all year round, which might not be realistic in large-scale applications. In accordance with previous investigations, we add constraints that the irrigation is implemented solely during the local time window of 6 A.M. to 10 A.M. to minimize evaporative losses (Ozdogan et al., 2010; Qian et al., 2013; B. Yang et al., 2016). Furthermore, the inclusion of winter cultivation necessitates the imposition of temperature limitation, as irrigation under freezing conditions is deemed impractical and detrimental to winter wheat (B. Yang et al., 2016). To make sure the soil is appropriate for irrigation, we check whether the mean temperature of the uppermost soil layer within the preceding 24-hour period exceeds 5°C. Additionally, we follow the rules from the default irrigation model that the irrigation can be promptly suspended in the presence of precipitation exceeding a threshold rate of 1mm/hr.

The default daily irrigation amount is resolved according to Equation (3) based on the soil moisture and vegetation fraction which is fixed to be 0.95. When adopting it to large-scale

irrigation, we replace the 0.95 with the irrigation land fraction (IRRFRA) map around 2005 from the Food Agriculture Organization database (Stefan Siebert et al., 2013).

$$\text{Default Irrigation Amount} = \int(\text{SMCLIM} - \text{SMCAVL}) * 0.95 \quad (3)$$

$$\text{Improved Irrigation Amount} = \int(\text{SMCLIM} - \text{SMCAVL}) * \text{IRRFRA} \quad (4)$$

Irrigation is required when the soil moisture is lower than the predefined irrigation threshold called management allowable deficit (MAD). MAD is a decimal number between 0 and 1, indicating the cursor between the wilting and the saturated soil moisture. Soil water deficit is the gap between current soil moisture availability (SMCAVL) and the expected soil moisture defined by the MAD (SMCLIM). The total irrigation amount is the integrated deficit of all soil layers. It is stated that the county-level calibrated irrigation threshold significantly enhances the irrigation prediction (Xu et al., 2019; Z. Zhang et al., 2020). Similarly, we calibrated the irrigation threshold province by province using the updated irrigation function, and finally apply this MAD spatial map to IRRnew experiment. As a comparison, IRRdef only adopts 0.8 as a uniform threshold which is simply calibrated by the national total amount (Yuwen Fan et al., 2023).

2.5 Modification of the groundwater model

Since the inclusion of lateral flow becomes crucial in predicting soil moisture in the western NCP due to the steep water table gradient along the mountainous region, we select the groundwater model from Miguez-Macho et al. (2007) which incorporates both water table dynamics and subsurface lateral flows, and then add the irrigation extraction to it. Irrigation is partially extracted from the groundwater (Equation 5) based on the reported groundwater dependence of each province (Figure 1e). Since the default groundwater only updates every 30 minutes instead of every timestep, the accumulated extraction amount during that timeframe is extracted all at once. And the groundwater table level is then recalculated based on new storage as well as the soil porosity.

$$\text{Groundwater} = \text{Groundwater} - \text{Total Irrigation} \times \text{Groundwater Dependence (\%)} \quad (5)$$

3 Results

3.1 Irrigation Simulation

It is a challenge to obtain a comprehensive and accurate observed irrigation map that covers the entirety of eastern China, thus, we combine the statistical data and the satellite data, considering the merged dataset as the 'observation' for calibration purposes. The statistical dataset is province-based, and it was collected in 2005 which well matches our experiments. However, it is provided as annual agricultural water usage which not only comprises irrigation, but also husbandry, forestry, and fishery consumption (National Bureau of Statistics of China, 2005). So firstly, agricultural water withdrawal (Figure 4b) is converted to net irrigation (Figure

4c) by multiplying the provincial ratios from Zhu et al. (2012). For better visualization, irrigation is redistributed to each crop grid based on the irrigation fraction (Figure 4a). In other words, the weighted provincial mean value of the redistribution map (Figure 4d) is the same as the statistical irrigation usage (Figure 4c). Surprisingly, in Figure 4d, the annual irrigation outside the NCP, such as southern coastal region, is much more intense than that in the NCP region, probably because it includes the great consumption used for raising rice in the extensive paddy field, which is not the main focus of this study. Another satellite-based irrigation dataset contains spatial maps retrieved from water balance equations orientally. Its irrigation amount (Figure 4e) has a high similarity with the irrigation land fraction, but it only covers 2011 to 2018 and it has a non-negligible underestimation (K. Zhang et al., 2022). Therefore, the statistical irrigation in the targeted NCP (i.e., Beijing, Tianjin, Hebei, Shandong, and Henan, follows D. Wu et al., 2018) is coupled with the satellite-based irrigation in other regions to be the final observation we used for calibration and validation (Figure 4f).

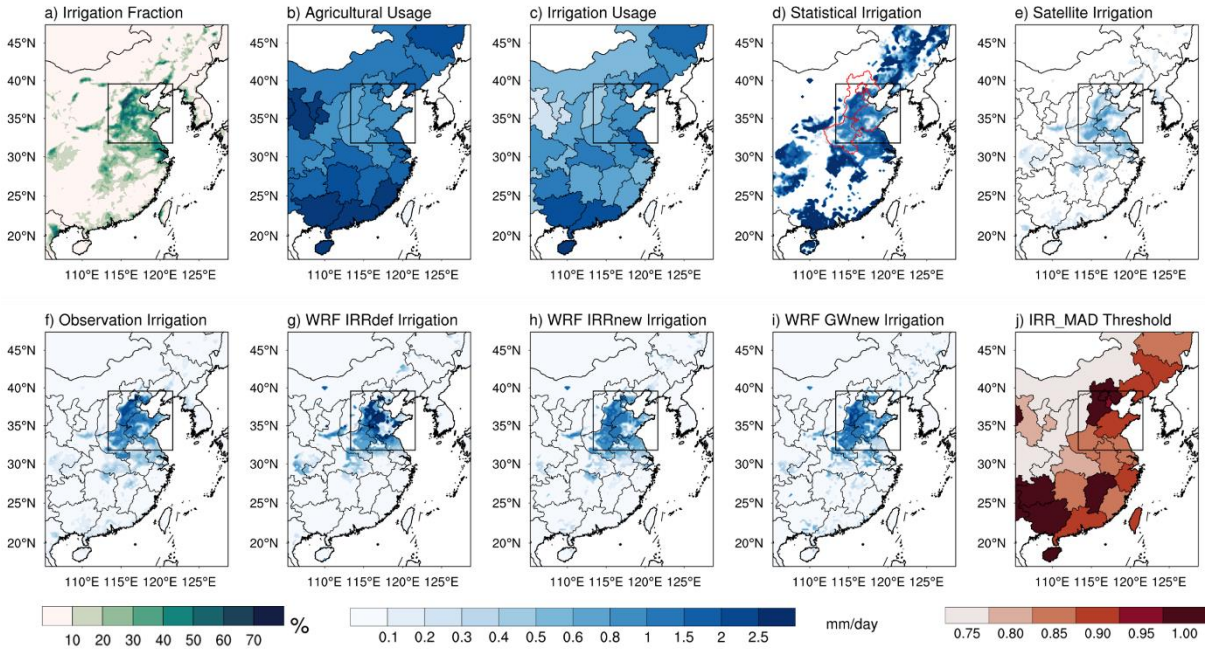

Figure 4. Spatial maps of (a) irrigation fraction (same as Figure 1d), (b) agricultural usage, (c) estimated irrigation usage, (d) statistical irrigation, e) satellite irrigation, f) observation irrigation, (g-i) simulated irrigation, and (j) MAD threshold adopted in IRRnew and GWnew

The default irrigation scheme (Figure 4g) exhibits a tendency to overestimate irrigation in the central NCP, deviating from the observed pattern where irrigation is more prevalent in the western part along the mountain. As expected, the implementation of the spatially varied irrigation threshold demonstrates a considerable improvement (Figure 4h), closely resembling the observed spatial variability. Figure 4(j) presents the province-based MAD threshold we adopted, which is calibrated using the observation. Certain provinces in the NCP exhibit higher thresholds, even approaching 1, indicating the model's attempt to achieve near-saturation of the soil. When comparing GWnew with IRRnew, the incorporation of the groundwater scheme helps to capture the greater irrigation requirement in the mountainous region. This can be

attributed to the deeper groundwater table and quicker dry-down after daily irrigation. The temporal pattern clearly emphasizes the importance of incorporating soil temperature checks into the irrigation scheme. In Figure 5, the lines depict the monthly irrigation levels, while the bars represent the averaged LAI across all crop grids in the NCP region. The default irrigation scheme tends to apply excessive irrigation during the winter season, which can be attributed to the relatively drier soil conditions and thus larger gap between the soil moisture and the MAD threshold. However, despite the intense winter irrigation, the corresponding vegetation growth, as indicated by the LAI, shows insignificant improvement. And this perceived superiority of winter irrigation gradually diminishes as spring approaches. On the other hand, the improved model effectively avoids unnecessary winter irrigation, allowing for a greater allocation of water resources during the spring and summer seasons when crop growth is more pronounced. Consequently, this strategic water distribution leads to more flourishing vegetation during the summer season. In summary, the improved model provides enhanced water support to the crops while also conserving irrigation consumption on an annual basis.

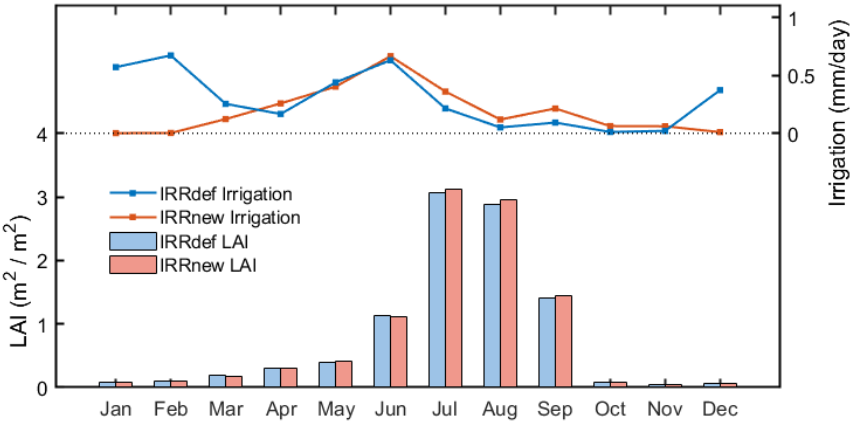

Figure 5. Monthly irrigation (lines) and LAI (bars) from IRRdef, IRRnew and GWnew. Only crop grids in the NCP are counted.

3.2 Evaluation of crop growth

The evaluation of the crop simulation encompasses several key aspects, including crop stage identification, annual cycle of leaf and stem mass, crop yield prediction, and general LAI simulation. These components will be scrutinized to assess the accuracy and validity of the crop model.

As mentioned, the heading and maturity dates serve as indicators of the transition from the vegetative stage to the reproductive stage, and ultimately to the maturity stage. We compare the heading and maturity dates of winter wheat and maize, including both summer maize and spring maize, from each simulation with the estimations derived from MODIS (Figure 6). Typically, winter wheat heads in March and matures in May, while maize heads in August and matures in September. The default crop model only considers single cropping without winter wheat. Moreover, the heading date of CROPdef is observed to be one or two months earlier than the observations, and the maturity date also exhibits deviations, being earlier in the NCP

but later in Northeast China. This suggests that employing a uniform starting and ending time is not suitable for a regional domain. The enhanced crop model, CROPnew, incorporates double cropping and spatially varied planting and harvesting dates, resulting in the presence of two seasons with a more accurate duration. This is because the adjustment allows for an earlier seeding and longer growing season for spring maize in the northern region, enabling the accumulation of the same Growing Degree Days (GDD) by the maturity season. The early bias is further mitigated by irrigation, as the presence of moist soil induces primary cooling, subsequently decelerating GDD accumulation and postponing the growth stage. Furthermore, the improvements made to the irrigation module and the integration of groundwater interaction slightly enhance the stage identification process, which is presented in the extended version of stage validation that includes all experiments (Figure S1).

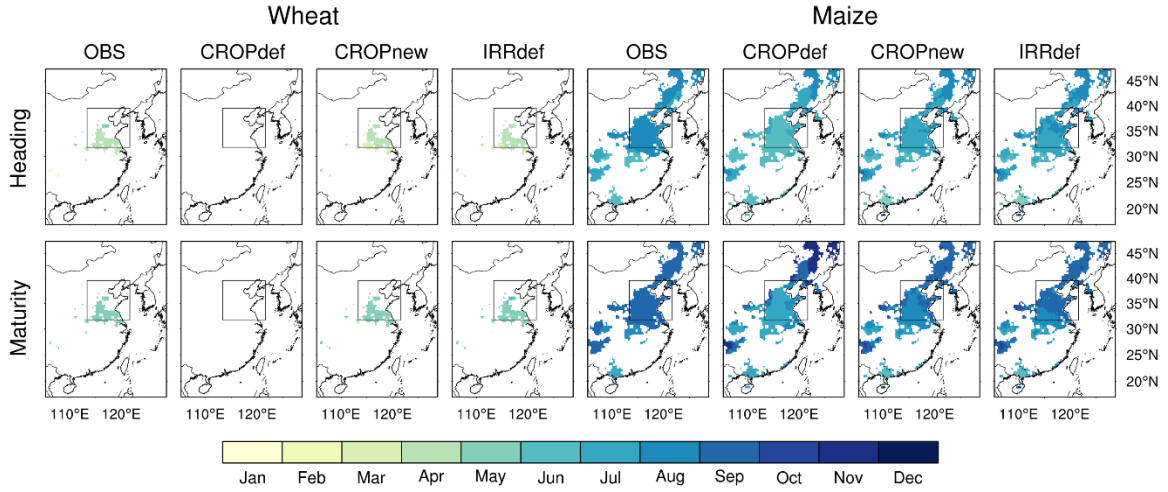

Figure 6. Validation of the crop stage identification by comparing the wheat heading date, wheat maturity date, maize heading date, maize maturity date between the simulations and the observation

When examining the annual biomass of the Yucheng station (Figure 7a and 7c), the biomass cycle exhibits two distinct peaks, representing two crop seasons. In alignment with Figure 6, applying irrigation extends the winter wheat growth, moving the peak to the right side and resulting in a better match with the observation. Furthermore, the upgrades of the irrigation model led to significant enhancements at the Yucheng station, particularly for summer maize. This aligns with the conclusions drawn from Figure 5, as well as the suboptimal maize growth under water stress conditions captured by another crop model (Song & Jin, 2020), further approving the positive influence of the improved irrigation model on crop growth. On the other hand, irrigation is not intensely adopted in northeast China, and thus, does not make a noticeable impact at Shenyang Station (Figure 7b and 7d). In addition, the impact of groundwater integration is not particularly pronounced in both stations, probably because groundwater impact is usually considered a long-term effect, and the one-year duration may not be sufficient to fully demonstrate its impact. And the 27km grid spacing may be insufficient

to capture the lateral dynamics of groundwater (Barlage et al., 2021), thus limiting the manifestation of groundwater's effect.

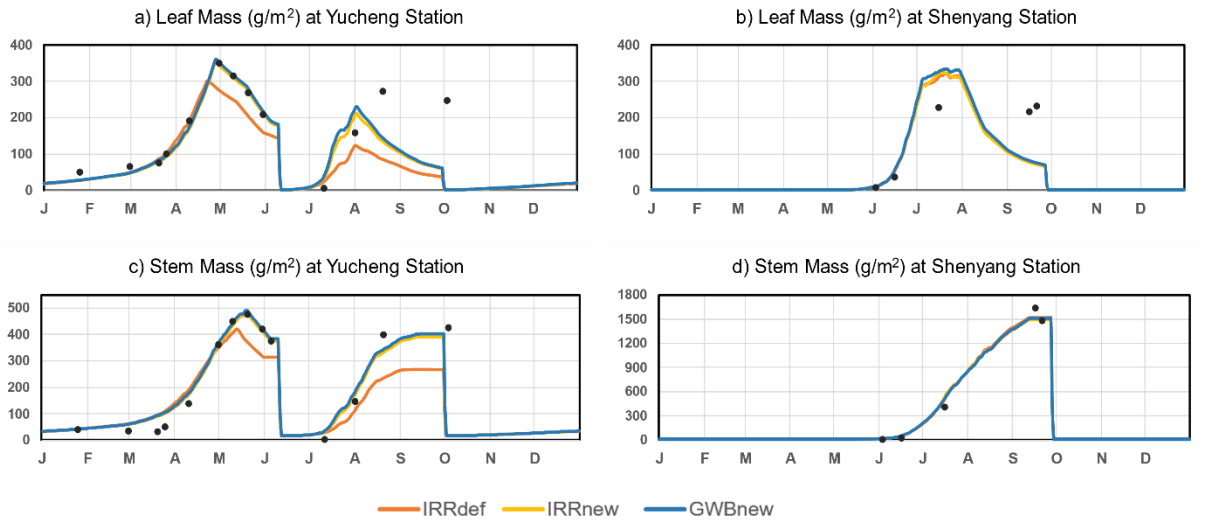

Figure 7. Validation of the annual cycle of leaf mass and stem mass at (a, c) Yucheng Station and (b, d) Shenyang Station. Dots represent station observation and lines are the simulation results.

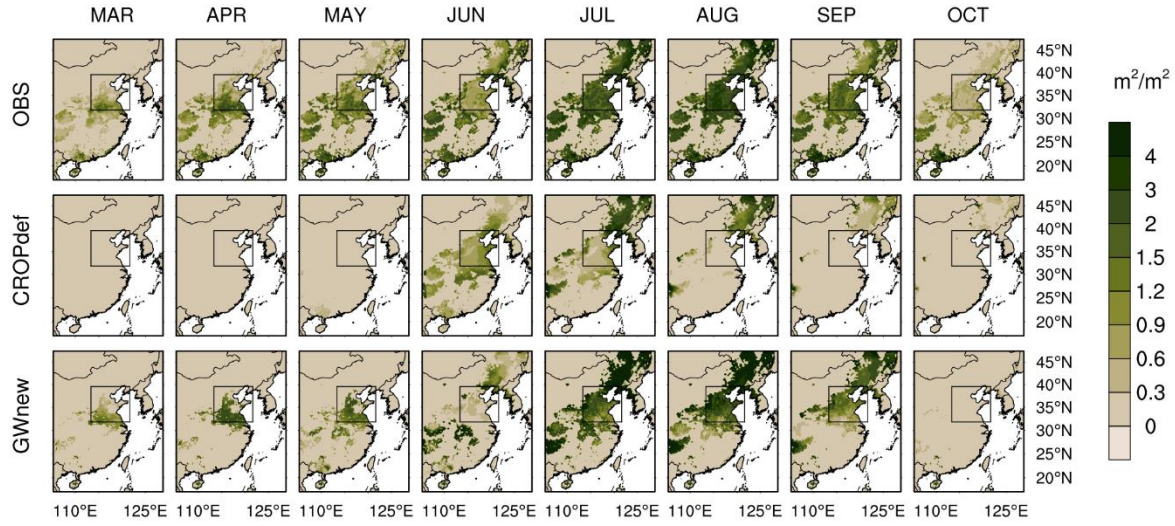

Figure 8. Validation of crop yield of wheat and maize.

By assessing the crop yield prediction in Figure 8, we can observe the progressive improvements achieved through model modification. The initial CROPdef only considers a single crop type, and it proves to be inadequate for the heavily irrigated NCP region, even with the exaggerated assumption of a fixed FVEG value of 0.95. Despite the recalibration of parameters and adjustments to the planting and harvesting dates, which realizes the double cropping simulations in the CROPnew, production in the NCP region is still severely hindered by the limited water availability. The activation of the default irrigation module in IRRdef, despite some imperfections, significantly promotes crop growth. This highlights the

importance of irrigation in sustaining the compact rotation and high productivity in the NCP. On the other hand, irrigation impact in northeast China is not as significant as that in the NCP, which aligns with the fact that the majority of the cropland in northeast China is rainfed. Similar to Figure 7, the improvement in irrigation practices further enhances crop yields, particularly for summer maize. The integration of groundwater results in only marginal improvement in the double cropping of summer corn, while it does not cause any significant deviations in the single cropping station.

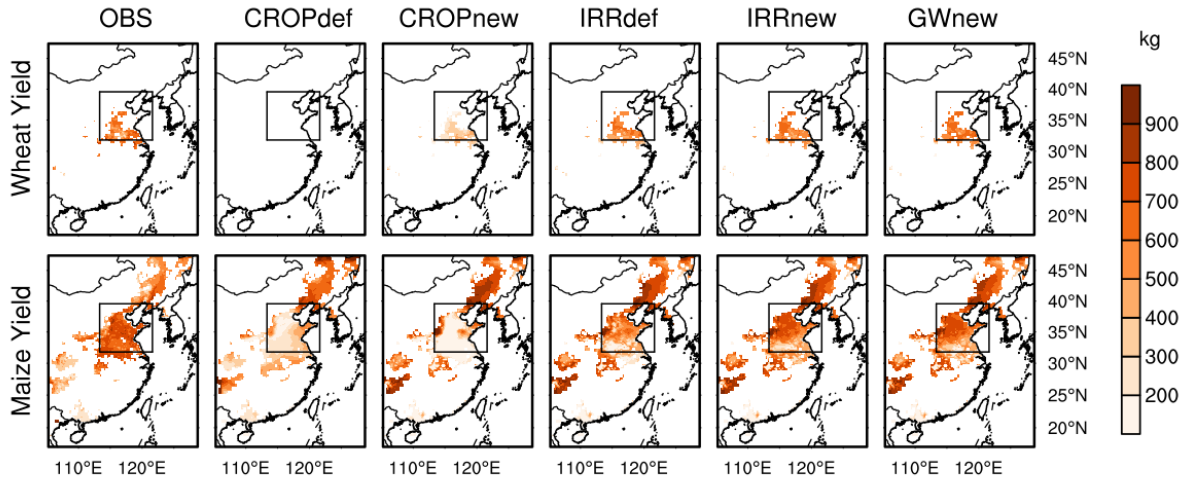

Figure 9. Monthly LAI pattern of the satellite observation, default crop model only, and after all modification and integration.

Finally, the validation of monthly LAI as an indicator of overall vegetation growth is essential, as its accuracy plays a crucial role in determining land-atmosphere interaction and energy partitioning (X. Liu et al., 2016). Figure 9 compares the simplest crop model and the final integrated system with observation, emphasizing the remarkable improvement achieved through the integration and regionalization processes. Figure S2 provides an extended version inclusive of all experiments, thoroughly visualizing the gradual improvement made by each step. The observed LAI demonstrates a gradual increase until May, with a slight decline in June, indicating the harvest of winter wheat. In the second crop season, there is a notable rise in LAI during July and August, reflecting substantial growth and vegetation development during this period, followed by a gradual decline in September and October. It becomes evident that the CROPdef lacks representation of the first crop season and exhibits an early and truncated second crop season in the NCP. The inclusion of irrigation, both in the IRRdef and IRRnew models, significantly enhances crop growth in the double cropping region, highlighting the crucial role of irrigation in this region. Conversely, the crops in Northeast China, where rain-fed agriculture predominates, exhibit reasonably satisfactory growth even without irrigation. This regional disparity in crop sensitivity to irrigation can be aptly captured by the improved system. In line with the previous figures, the IRRnew proves particularly beneficial for the growth of summer maize. Its avoidance of unnecessary irrigation during the freezing winter months allows for greater resource allocation during the productive summer period, resulting in improved growth and development. Generally, the GWnew simulation successfully captures

the spatial and temporal LAI patterns, particularly in the NCP region, which demonstrates a superior capability in accurately representing the dynamics of crop growth compared to the initial crop model, which lacked regionalization and integration. In addition to the LAI, the joint crop modelling system also demonstrates reasonable predictability in monthly FVEG (Figure S3). Consequently, this expanded functionality offers valuable opportunities to conduct sensitivity tests, enabling a deeper understanding of the agriculture-related climate response.

4 Discussion and conclusion

Considering the close and complex connections between crop growth, irrigation application and groundwater interaction in the NCP, the development of a comprehensive crop-irrigation-groundwater model becomes necessary for accurate prediction of crop growth in this region. The objective of this study is to create an integrated crop model that incorporates irrigation and groundwater interactions in the regional climate model, specifically designed for the NCP and its surrounding areas. The inclusion of the prevalent double cropping rotation enables a much more accurate simulation of plant phenology and irrigation practices. This improved system can further be applied in long-term simulations to understand the agricultural-related climate response.

The interconnections between the various models are depicted in Figure 10. In the default Noah-MP Land Surface Model (LSM), all modules are linked with the surface soil, but direct connections between them are absent. By introducing direct interactions between these schemes and regionalizing the functions and parameters, the integrated crop modelling system demonstrates its overall reasonable ability to predict crop production based on climatic conditions. This is validated through the accurate identification of crop stages, field point biomass estimation, crop yield prediction, and the monthly LAI pattern. The integration of these components enhances the model's predictability and allows for a more comprehensive understanding of crop growth dynamics in the NCP.

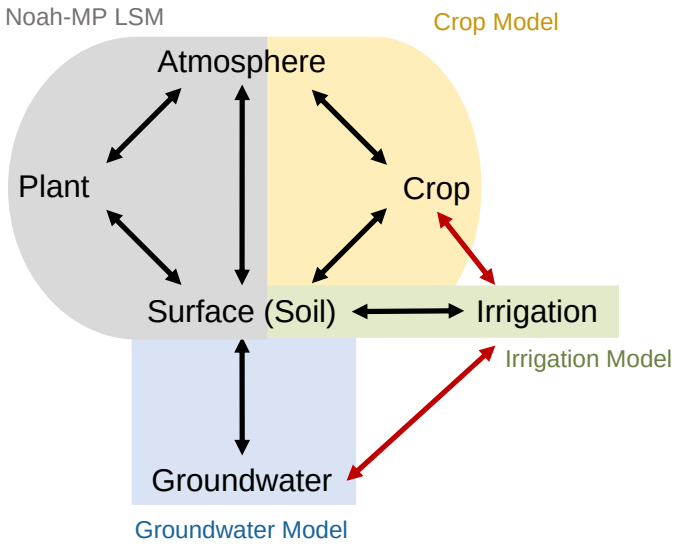

Figure 10. How models are connected. Red arrows are new connections added in this study.

Nevertheless, the validation process has brought to light several limitations of the current model. To start with, the model design restricts the simulation of only one crop type per grid. This simplification may contribute to inaccuracies in predicting the leaf mass of summer maize at the Yucheng Station, which can be revealed by the inconsistency of LAI observation (Figure 9) in the NCP region and the leaf mass at the Yucheng Station (Figure 7). While the LAI values indicate that September should have a smaller LAI compared to July, the station data suggests that September actually has a greater leaf mass than July. This discrepancy can be attributed to two factors. Firstly, the specific leaf area, or BIO2LAI in the model, varies across different crop stages, as supported by both station data and existing literature (Amanullah, 2015; H. Zhou et al., 2020). In other words, the leaves may be thinner and broader in July, while they become thicker and heavier in September. The second reason is that the observed LAI pattern represents a spatial average value over the grid, which may contain a diverse range of crops. Consequently, the specific station data for summer maize may not align well with the spatially averaged LAI. Since this study primarily focuses on the regional scale rather than individual field points, we prioritize matching the spatial LAI pattern while partially sacrificing the accuracy in predicting station leaf mass. As a result, the simulated LAI pattern is well-matched in the NCP region, while the predicted leaf mass for summer maize may not closely align with the station data. On the contrary, winter wheat greatly, even exclusively dominates the first crop season, and thus the station data and spatial pattern are consistent and can both be captured by the model. Also, the predicted LAI completely cleared up after harvesting, since each grid can only predict one type of growth pattern, which is different from the gradual fading observed in June and October.

Additionally, it is important to acknowledge that the model performance may be less satisfactory in regions outside the primary focus of the NCP. There is some underestimation of LAI and yield in the southern boundary of the NCP, as well as the overestimation in northeast China. This could potentially be attributed to the limited predictability of FVEG. Also, considering their different crop rotations and crop types to the NCP, the current crop system may not be adequate to capture the LAI dynamics in the south coastal region and southwest China. Even in regions where the model currently exhibits reasonable performance, uncertainty can arise from the model's sensitivity to soil moisture (G. Wang, 2005). For instance, this study only conducts experiments in a normal year, its performance in dry years or wet years needs to be further tested.

Overall, our study has already demonstrated reasonable performance of this regional-scale application in somewhere with a totally distinct climate background from the central US, where the model originally developed. This implies the potential for applying it in other agricultural zones. And most of our validation data is derived from satellite observations, indicating the possibility of adopting it in regions even with limited ground-based data. Also, the integrated crop system clearly highlights the significance of an appropriate irrigation scheme in the NCP region. The inclusion of the groundwater model enables a more precise representation of the spatial irrigation pattern, particularly along the mountain where irrigation is more intensified. However, it does not yield significant differences, particularly in terms of crop growth. Nevertheless, it is crucial to note that within the span of one year, the water exchange between

the soil and groundwater already influences the irrigation pattern, suggesting that over a longer period, as groundwater gradually depletes, there may be more substantial changes in the hydrological cycle. Further research will focus on utilizing this crop system in long-term simulations, with an emphasis on investigating the cultivation-induced climate impacts and hydrological changes, including groundwater storage.

Acknowledgments

This study was supported by the Hong Kong Research Grants Council funded project, GRF16309719. We would like to give special thanks to Dr. Ben Yang for providing his irrigation model as a reference.

Data Availability Statement

The climatology precipitation is retrieved from the China Meteorological Forcing Dataset and is adopted for precipitation validation. It is produced by Cold and Arid Regions Science Data Center, with doi:10.3972/westdc.002.2014.db, published at http://westdc.westgis.ac.cn. East Asian Summer Monsoon Index is referred to http://lijianping.cn/dct/page/65577, with the definition from Li and Zeng (Li & Zeng, 2002). LAI dataset is initially Sun Yat-sen University (Yuan et al., 2020), shown at http://globalchange.bnu.edu.cn/data/global_lai_0.1/. The cropping pattern is defined by ChinaCP (Qiu et al., 2022), available at https://doi.org/10.6084/m9.figshare.14936052. The planting and harvesting date is from the ChinaCropPhen1km dataset (Luo et al., 2020) at https://doi.org/10.6084/m9.figshare.8313530). Station data at Yucheng and Shenyang is provided by the National Ecosystem Research Network of China, and the yield data (Cheng et al., 2022) is freely available from https://doi.org/10.5281/zenodo.5121842.

References

Ahmed, K. F., Wang, G., Yu, M., Koo, J., & You, L. (2015). Potential impact of climate change on cereal crop yield in West Africa. *Climatic Change*, *133*(2), 321–334. https://doi.org/10.1007/s10584-015-1462-7

Amanullah. (2015). Specific Leaf Area and Specific Leaf Weight in Small Grain Crops Wheat, Rye, Barley, and Oats Differ at Various Growth Stages and NPK Source. *Journal of Plant Nutrition*, *38*(11), 1694–1708. https://doi.org/10.1080/01904167.2015.1017051

An, L., Wang, J., Huang, J., Pokhrel, Y., Hugonnet, R., Wada, Y., et al. (2021). Divergent Causes of Terrestrial Water Storage Decline Between Drylands and Humid Regions Globally. *Geophysical Research Letters*, *48*(23), e2021GL095035. https://doi.org/10.1029/2021GL095035

Anderson, R. G., Lo, M.-H., Swenson, S., Famiglietti, J. S., Tang, Q., Skaggs, T. H., et al. (2015). Using satellite-based estimates of evapotranspiration and groundwater changes

664 to determine anthropogenic water fluxes in land surface models. *Geoscientific Model*
665 *Development*, *8*(10), 3021–3031. https://doi.org/10.5194/gmd-8-3021-2015
666 Barlage, M., Chen, F., Rasmussen, R., Zhang, Z., & Miguez-Macho, G. (2021). The
667 Importance of Scale-Dependent Groundwater Processes in Land-Atmosphere
668 Interactions Over the Central United States. *Geophysical Research Letters*, *48*(5),
669 e2020GL092171. https://doi.org/10.1029/2020GL092171
670 Cheng, M., Jiao, X., Shi, L., Penuelas, J., Kumar, L., Nie, C., et al. (2022). High-resolution
671 crop yield and water productivity dataset generated using random forest and remote
672 sensing. *Scientific Data*, *9*(1), 641. https://doi.org/10.1038/s41597-022-01761-0
673 Cook, B. I., Puma, M. J., & Krakauer, N. Y. (2011). Irrigation induced surface cooling in the
674 context of modern and increased greenhouse gas forcing. *Climate Dynamics*, *37*(7–8),
675 1587–1600. https://doi.org/10.1007/s00382-010-0932-x
676 Dudhia, J. (1989). Numerical Study of Convection Observed during the Winter Monsoon
677 Experiment Using a Mesoscale Two-Dimensional Model. *Journal of the Atmospheric*
678 *Sciences*, *46*(20), 3077–3107. https://doi.org/10.1175/1520-
679 0469(1989)046<3077:NSOCOD>2.0.CO;2
680 Ek, M. B., Mitchell, K. E., Lin, Y., Rogers, E., Grunmann, P., Koren, V., et al. (2003).
681 Implementation of Noah land surface model advances in the National Centers for
682 Environmental Prediction operational mesoscale Eta model. *Journal of Geophysical*
683 *Research: Atmospheres*, *108*(D22), 2002JD003296.
684 https://doi.org/10.1029/2002JD003296
685 Famiglietti, J. S. (2014). The global groundwater crisis. *Nature Climate Change*, *4*(11), 945–
686 948. https://doi.org/10.1038/nclimate2425
687 Fan, Ying, Miguez-Macho, G., Weaver, C. P., Walko, R., & Robock, A. (2007). Incorporating
688 water table dynamics in climate modeling: 1. Water table observations and equilibrium
689 water table simulations: WATER TABLE OBSERVATIONS. *Journal of Geophysical*
690 *Research: Atmospheres*, *112*(D10). https://doi.org/10.1029/2006JD008111
691 Fan, Yuwen, Im, E.-S., Lan, C.-W., & Lo, M.-H. (2023). An increase in precipitation driven
692 by irrigation over the North China Plain based on RegCM and WRF simulations.
693 *Journal of Hydrometeorology*. https://doi.org/10.1175/JHM-D-22-0131.1
694 FAO. (2019). Food and Agriculture Organization Statistic Data. Retrieved from
695 http://www.fao.org/faostat/en/#compare
696 Foley, J. A., Ramankutty, N., Brauman, K. A., Cassidy, E. S., Gerber, J. S., Johnston, M., et al.
697 (2011). Solutions for a cultivated planet. *Nature*, *478*(7369), 337–342.
698 https://doi.org/10.1038/nature10452
699 Goldewijk, K. K. (2001). Estimating global land use change over the past 300 years: The
700 HYDE Database. *Global Biogeochemical Cycles*, *15*(2), 417–433.
701 https://doi.org/10.1029/1999GB001232
702 Han, J., & Pan, H.-L. (2011). Revision of Convection and Vertical Diffusion Schemes in the
703 NCEP Global Forecast System. *Weather and Forecasting*, *26*(4), 520–533.
704 https://doi.org/10.1175/WAF-D-10-05038.1
705 He, C., Valayamkunnath, P., Barlage, M., Chen, F., Gochis, D., Cabell, R., et al. (2023). *The*
706 *Community Noah-MP Land Surface Modeling System Technical Description Version*
707 *5.0*. NCAR Technical Note NCAR/TN-575+ STR, doi: 10.5065/ew8g-yr95.

Hersbach, H., Bell, B., Berrisford, P., Hirahara, S., Horányi, A., Muñoz-Sabater, J., et al. (2020). The ERA5 global reanalysis. *Quarterly Journal of the Royal Meteorological Society*, *146*(730), 1999–2049. https://doi.org/10.1002/qj.3803

Hong, S.-Y., Dudhia, J., & Chen, S.-H. (2004). A Revised Approach to Ice Microphysical Processes for the Bulk Parameterization of Clouds and Precipitation. *Monthly Weather Review*, *132*(1), 103–120. https://doi.org/10.1175/1520-0493(2004)132<0103:ARATIM>2.0.CO;2

Hong, S.-Y., Noh, Y., & Dudhia, J. (2006). A New Vertical Diffusion Package with an Explicit Treatment of Entrainment Processes. *Monthly Weather Review*, *134*(9), 2318–2341. https://doi.org/10.1175/MWR3199.1

Huang, H., Huang, J., Li, X., Zhuo, W., Wu, Y., Niu, Q., et al. (2022). A dataset of winter wheat aboveground biomass in China during 2007–2015 based on data assimilation. *Scientific Data*, *9*(1), 200. https://doi.org/10.1038/s41597-022-01305-6

Huang, X., Wang, C., Hou, J., Du, C., Liu, S., Kang, J., et al. (2020). Coordination of carbon and nitrogen accumulation and translocation of winter wheat plant to improve grain yield and processing quality. *Scientific Reports*, *10*(1), 10340. https://doi.org/10.1038/s41598-020-67343-5

Im, E.-S., Marcella, M. P., & Eltahir, E. A. B. (2014). Impact of Potential Large-Scale Irrigation on the West African Monsoon and Its Dependence on Location of Irrigated Area. *Journal of Climate*, *27*(3), 994–1009. https://doi.org/10.1175/JCLI-D-13-00290.1

Jiang, Y., Yin, X., Wang, X., Zhang, L., Lu, Z., Lei, Y., et al. (2021). Impacts of global warming on the cropping systems of China under technical improvements from 1961 to 2016. *Agronomy Journal*, *113*(1), 187–199. https://doi.org/10.1002/agj2.20497

Kabir, T., Pokhrel, Y., & Felfelani, F. (2023). Climatic and anthropogenic controls on groundwater dynamics in the Mekong River Basin. *Journal of Hydrology*, *622*, 129761. https://doi.org/10.1016/j.jhydrol.2023.129761

Kang, S., & Eltahir, E. A. B. (2018). North China Plain threatened by deadly heatwaves due to climate change and irrigation. *Nature Communications*, *9*(1), 2894. https://doi.org/10.1038/s41467-018-05252-y

Kang, S., & Eltahir, E. A. B. (2019). Impact of Irrigation on Regional Climate Over Eastern China. *Geophysical Research Letters*, *46*(10), 5499–5505. https://doi.org/10.1029/2019GL082396

Koch, J., Zhang, W., Martinsen, G., He, X., & Stisen, S. (2020). Estimating Net Irrigation Across the North China Plain Through Dual Modeling of Evapotranspiration. *Water Resources Research*, *56*(12). https://doi.org/10.1029/2020WR027413

Kwon, Y. C., & Hong, S.-Y. (2017). A Mass-Flux Cumulus Parameterization Scheme across Gray-Zone Resolutions. *Monthly Weather Review*, *145*(2), 583–598. https://doi.org/10.1175/MWR-D-16-0034.1

Leng, G., Huang, M., Tang, Q., Gao, H., & Leung, L. R. (2014). Modeling the Effects of Groundwater-Fed Irrigation on Terrestrial Hydrology over the Conterminous United States. *Journal of Hydrometeorology*, *15*(3), 957–972. https://doi.org/10.1175/JHM-D-13-049.1

Li, J., & Zeng, Q. (2002). A unified monsoon index. *Geophysical Research Letters*, *29*(8). https://doi.org/10.1029/2001GL013874

Liu, W., Wang, G., Yu, M., Chen, H., Jiang, Y., Yang, M., & Shi, Y. (2020). Projecting the future vegetation–climate system over East Asia and its RCP-dependence. *Climate Dynamics*, *55*(9–10), 2725–2742. https://doi.org/10.1007/s00382-020-05411-2

Liu, X., Chen, F., Barlage, M., Zhou, G., & Niyogi, D. (2016). Noah-MP-Crop: Introducing dynamic crop growth in the Noah-MP land surface model: Noah-MP-Crop. *Journal of Geophysical Research: Atmospheres*, *121*(23), 13,953-13,972. https://doi.org/10.1002/2016JD025597

Lo, M.-H., & Famiglietti, J. S. (2011). Precipitation response to land subsurface hydrologic processes in atmospheric general circulation model simulations. *Journal of Geophysical Research*, *116*(D5), D05107. https://doi.org/10.1029/2010JD015134

Lo, M.-H., Wey, H.-W., Im, E.-S., Tang, L. I., Anderson, R. G., Wu, R.-J., et al. (2021). Intense agricultural irrigation induced contrasting precipitation changes in Saudi Arabia. *Environmental Research Letters*, *16*(6), 064049. https://doi.org/10.1088/1748-9326/ac002e

Luo, Y., Zhang, Z., Chen, Y., Li, Z., & Tao, F. (2020). ChinaCropPhen1km: a high-resolution crop phenological dataset for three staple crops in China during 2000–2015 based on leaf area index (LAI) products. *Earth System Science Data*, *12*(1), 197–214. https://doi.org/10.5194/essd-12-197-2020

Ma, Q., Cui, Z., & Huang, Y. (2006). Study on the Dry Matter Increase Allocation Ratio of Winter Wheat. *Meteorological and Environmental Sciences*, (4), 50–51.

McDermid, S., Nocco, M., Lawston-Parker, P., Keune, J., Pokhrel, Y., Jain, M., et al. (2023). Irrigation in the Earth system. *Nature Reviews Earth & Environment*, *4*(7), 435–453. https://doi.org/10.1038/s43017-023-00438-5

Miguez-Macho, G., Fan, Y., Weaver, C. P., Walko, R., & Robock, A. (2007). Incorporating water table dynamics in climate modeling: 2. Formulation, validation, and soil moisture simulation. *Journal of Geophysical Research: Atmospheres*, *112*(D13), 2006JD008112. https://doi.org/10.1029/2006JD008112

Mlawer, E. J., Taubman, S. J., Brown, P. D., Iacono, M. J., & Clough, S. A. (1997). Radiative transfer for inhomogeneous atmospheres: RRTM, a validated correlated-k model for the longwave. *Journal of Geophysical Research: Atmospheres*, *102*(D14), 16663–16682. https://doi.org/10.1029/97JD00237

National Bureau of Statistics of China. (2005). *China Statistical Yearbook*. Beijing. Retrieved from http://www.stats.gov.cn/tjsj/ndsj/2005/indexeh.htm

Niu, G.-Y., Yang, Z.-L., Dickinson, R. E., Gulden, L. E., & Su, H. (2007). Development of a simple groundwater model for use in climate models and evaluation with Gravity Recovery and Climate Experiment data. *Journal of Geophysical Research*, *112*(D7), D07103. https://doi.org/10.1029/2006JD007522

Niu, G.-Y., Yang, Z.-L., Mitchell, K. E., Chen, F., Ek, M. B., Barlage, M., et al. (2011). The community Noah land surface model with multiparameterization options (Noah-MP): 1. Model description and evaluation with local-scale measurements. *Journal of Geophysical Research*, *116*(D12), D12109. https://doi.org/10.1029/2010JD015139

Oleson, K., Lawrence, D., Bonan, G., Drewniak, B., Huang, M., Koven, C., et al. (2013). *Technical description of version 4.5 of the Community Land Model (CLM)* [Application/pdf] (p. 5912 KB). UCAR/NCAR. https://doi.org/10.5065/D6RR1W7M

Ozdogan, M., Rodell, M., Beaudoing, H. K., & Toll, D. L. (2010). Simulating the Effects of Irrigation over the United States in a Land Surface Model Based on Satellite-Derived Agricultural Data. *Journal of Hydrometeorology*, *11*(1), 171–184. https://doi.org/10.1175/2009JHM1116.1

Pei, L., Moore, N., Zhong, S., Kendall, A. D., Gao, Z., & Hyndman, D. W. (2016). Effects of irrigation on summer precipitation over the United States. *Journal of Climate*, *29*(10), 3541–3558.

Pokhrel, Y., Hanasaki, N., Koirala, S., Cho, J., Yeh, P. J.-F., Kim, H., et al. (2012). Incorporating Anthropogenic Water Regulation Modules into a Land Surface Model. *Journal of Hydrometeorology*, *13*(1), 255–269. https://doi.org/10.1175/JHM-D-11-013.1

Portmann, F. T., Siebert, S., & Döll, P. (2010). MIRCA2000-Global monthly irrigated and rainfed crop areas around the year 2000: A new high-resolution data set for agricultural and hydrological modeling: MONTHLY IRRIGATED AND RAINFED CROP AREAS. *Global Biogeochemical Cycles*, *24*(1), n/a-n/a. https://doi.org/10.1029/2008GB003435

Puma, M. J., & Cook, B. I. (2010). Effects of irrigation on global climate during the 20th century. *Journal of Geophysical Research*, *115*(D16), D16120. https://doi.org/10.1029/2010JD014122

Qian, Y., Huang, M., Yang, B., & Berg, L. K. (2013). A Modeling Study of Irrigation Effects on Surface Fluxes and Land–Air–Cloud Interactions in the Southern Great Plains. *Journal of Hydrometeorology*, *14*(3), 700–721. https://doi.org/10.1175/JHM-D-12-0134.1

Qiu, B., Hu, X., Chen, C., Tang, Z., Yang, P., Zhu, X., et al. (2022). Maps of cropping patterns in China during 2015–2021. *Scientific Data*, *9*(1), 479. https://doi.org/10.1038/s41597-022-01589-8

Siebert, S., Burke, J., Faures, J. M., Frenken, K., Hoogeveen, J., Döll, P., & Portmann, F. T. (2010). Groundwater use for irrigation – a global inventory. *Hydrology and Earth System Sciences*, *14*(10), 1863–1880. https://doi.org/10.5194/hess-14-1863-2010

Siebert, Stefan, Henrich, V., Frenken, K., & Burke, J. (2013). Global Map of Irrigation Areas version 5 [Data set]. Rheinische Friedrich-Wilhelms-University, Bonn, Germany / Food and Agriculture Organization of the United Nations. https://doi.org/10.13019/M20599

Song, L., & Jin, J. (2020). Improving CERES-Maize for simulating maize growth and yield under water stress conditions. *European Journal of Agronomy*, *117*, 126072. https://doi.org/10.1016/j.eja.2020.126072

Tuinenburg, O. A., Hutjes, R. W. A., Stacke, T., Wiltshire, A., & Lucas-Picher, P. (2014). Effects of Irrigation in India on the Atmospheric Water Budget. *Journal of Hydrometeorology*, *15*(3), 1028–1050. https://doi.org/10.1175/JHM-D-13-078.1

Valayamkunnath, P., Chen, F., Barlage, M. J., Gochis, D. J., Franz, K. J., & Cosgrove, B. A. (2021). Impact of Agriculture Management Practices on the National Water Model Simulated Streamflow. Presented at the 101st American Meteorological Society Annual Meeting, AMS. Retrieved from https://ams.confex.com/ams/101ANNUAL/meetingapp.cgi/Paper/383317

Vira, J., Hess, P., Melkonian, J., & Wieder, W. R. (2019). *An improved mechanistic model for ammonia volatilization in Earth system models: Flow of Agricultural Nitrogen, version 2 (FANv2)* (preprint). Biogeosciences. https://doi.org/10.5194/gmd-2019-233

Wada, Y., van Beek, L. P. H., & Bierkens, M. F. P. (2012). Nonsustainable groundwater sustaining irrigation: A global assessment. *Water Resources Research*, *48*(6). https://doi.org/10.1029/2011WR010562

Wang, D., Wang, G., & Anagnostou, E. N. (2007). Evaluation of canopy interception schemes in land surface models. *Journal of Hydrology*, *347*(3–4), 308–318. https://doi.org/10.1016/j.jhydrol.2007.09.041

Wang, E., Yu, Q., Wu, D., & Xia, J. (2008). Climate, agricultural production and hydrological balance in the North China Plain. *International Journal of Climatology*, *28*(14), 1959–1970. https://doi.org/10.1002/joc.1677

Wang, G. (2005). Agricultural drought in a future climate: results from 15 global climate models participating in the IPCC 4th assessment. *Climate Dynamics*, *25*(7–8), 739–753. https://doi.org/10.1007/s00382-005-0057-9

Wang, J., Yang, Y., Huang, J., & Adhikari, B. (2019). Adaptive irrigation measures in response to extreme weather events: empirical evidence from the North China plain. *Regional Environmental Change*, *19*(4), 1009–1022. https://doi.org/10.1007/s10113-018-1442-3

Wang, L., Xie, Z., Xie, J., Zeng, Y., Liu, S., Jia, B., et al. (2020). Implementation of Groundwater Lateral Flow and Human Water Regulation in CAS-FGOALS-g3. *Journal of Geophysical Research: Atmospheres*, *125*(18). https://doi.org/10.1029/2019JD032289

Wang, S., Yongguang Zhang, & Weimin Ju. (2020). Long-term (1982-2018) global gross primary production dataset based on NIRv [Data set]. figshare. https://doi.org/10.6084/M9.FIGSHARE.12981977.V2

Wey, H.-W., Lo, M.-H., Lee, S.-Y., Yu, J.-Y., & Hsu, H.-H. (2015). Potential impacts of wintertime soil moisture anomalies from agricultural irrigation at low latitudes on regional and global climates: Remote Impact of Low-Latitude Irrigation. *Geophysical Research Letters*, *42*(20), 8605–8614. https://doi.org/10.1002/2015GL065883

Wu, D., Wang, C., Wang, F., Jiang, C., Huo, Z., & Wang, P. (2018). Uncertainty in Simulating the Impact of Cultivar Improvement on Winter Wheat Phenology in the North China Plain. *Journal of Meteorological Research*, *32*(4), 636–647. https://doi.org/10.1007/s13351-018-7139-1

Wu, L., Feng, J., & Miao, W. (2018). Simulating the Impacts of Irrigation and Dynamic Vegetation Over the North China Plain on Regional Climate. *Journal of Geophysical Research: Atmospheres*. https://doi.org/10.1029/2017JD027784

Wu, W., Yang, P., Tang, H., Zhou, Q., Chen, Z., & Shibasaki, R. (2010). Characterizing Spatial Patterns of Phenology in Cropland of China Based on Remotely Sensed Data. *Agricultural Sciences in China*, *9*(1), 101–112. https://doi.org/10.1016/S1671-2927(09)60073-0

Xu, X., Chen, F., Barlage, M., Gochis, D., Miao, S., & Shen, S. (2019). Lessons Learned From Modeling Irrigation From Field to Regional Scales. *Journal of Advances in Modeling Earth Systems*, *11*(8), 2428–2448. https://doi.org/10.1029/2018MS001595

Yan, H., Xiao, X., Huang, H., Liu, J., Chen, J., & Bai, X. (2014). Multiple cropping intensity in China derived from agro-meteorological observations and MODIS data. *Chinese Geographical Science*, *24*(2), 205–219. https://doi.org/10.1007/s11769-013-0637-2

Yang, B., Zhang, Y., Qian, Y., Tang, J., & Liu, D. (2016). Climatic effects of irrigation over the Huang-Huai-Hai Plain in China simulated by the weather research and forecasting model: Simulated Irrigation Effects in China. *Journal of Geophysical Research: Atmospheres*, *121*(5), 2246–2264. https://doi.org/10.1002/2015JD023736

Yang, M., & Wang, G. (2023). Heat stress to jeopardize crop production in the US Corn Belt based on downscaled CMIP5 projections. *Agricultural Systems*, *211*, 103746. https://doi.org/10.1016/j.agsy.2023.103746

Yang, Z., Dominguez, F., Zeng, X., Hu, H., Gupta, H., & Yang, B. (2017). Impact of Irrigation over the California Central Valley on Regional Climate. *Journal of Hydrometeorology*, *18*(5), 1341–1357. https://doi.org/10.1175/JHM-D-16-0158.1

Yang, Z., Qian, Y., Liu, Y., Berg, L. K., Hu, H., Dominguez, F., et al. (2019). Irrigation Impact on Water and Energy Cycle During Dry Years Over the United States Using Convection-Permitting WRF and a Dynamical Recycling Model. *Journal of Geophysical Research: Atmospheres*, *124*(21), 11220–11241. https://doi.org/10.1029/2019JD030524

Yang, Z., Qian, Y., Liu, Y., Berg, L. K., Gustafson, W. I., Feng, Z., et al. (2020). Understanding irrigation impacts on low-level jets over the Great Plains. *Climate Dynamics*, *55*(3–4), 925–943. https://doi.org/10.1007/s00382-020-05301-7

Yin, X., & van Laar, H. H. (2005). *Crop Systems Dynamics: An ecophysiological simulation model of genotype-by-environment interactions*. Wageningen Academic Publishers.

Yu, L., Liu, Y., Liu, T., Yu, E., Bu, K., Jia, Q., et al. (2022). Coupling localized Noah-MP-Crop model with the WRF model improved dynamic crop growth simulation across Northeast China. *Computers and Electronics in Agriculture*, *201*, 107323. https://doi.org/10.1016/j.compag.2022.107323

Yuan, H., Dai, Y., & Li, S. (2020). Reprocessed MODIS Version 6 Leaf Area Index data sets for land surface and climate modelling. Sun Yat-sun University.

Zeng, Y., Xie, Z., Liu, S., Xie, J., Jia, B., Qin, P., & Gao, J. (2018). Global Land Surface Modeling Including Lateral Groundwater Flow. *Journal of Advances in Modeling Earth Systems*, *10*(8), 1882–1900. https://doi.org/10.1029/2018MS001304

Zhang, K., Li, X., Zheng, D., Zhang, L., & Zhu, G. (2022). Estimation of Global Irrigation Water Use by the Integration of Multiple Satellite Observations. *Water Resources Research*, *58*(3). https://doi.org/10.1029/2021WR030031

Zhang, Y., Tao, B., & Tang, Z. (1991). A Simulation Model for the Growth and Development of Winter Wheat 冬小麦生长发育的模拟模式. *Transactions of Atmospheric Science 南京气象学院学报*, *14*(1), 113–121.

Zhang, Z., Barlage, M., Chen, F., Li, Y., Helgason, W., Xu, X., et al. (2020). Joint Modeling of Crop and Irrigation in the central United States Using the Noah-MP Land Surface Model. *Journal of Advances in Modeling Earth Systems*, *12*(7). https://doi.org/10.1029/2020MS002159

Zhang, Z., Li, Y., Chen, F., Harder, P., Helgason, W., Famiglietti, J., et al. (2023). Developing Spring Wheat in the Noah-MP LSM (v4.4) for Growing Season Dynamics and Responses to Temperature Stress. *Geoscientific Model Development Discussions*, 1–26. https://doi.org/10.5194/gmd-2022-311

Zhe, Y., Denghua, Y. a. N., Zhiyong, Y., Jun, Y. I. N., & Yong, Y. (2014). Research on temporal and spatial change of 400 mm and 800 mm rainfall contours of China in 1961-2000. 水科学进展, *25*(4), 494–502.

Zhou, H., Zhou, G., He, Q., Zhou, L., Ji, Y., & Zhou, M. (2020). Environmental explanation of maize specific leaf area under varying water stress regimes. *Environmental and Experimental Botany*, *171*, 103932. https://doi.org/10.1016/j.envexpbot.2019.103932

Zhou, Y., Dong, J., Cui, Y., Zhou, S., Li, Z., Wang, X., et al. (2022). Rapid surface water expansion due to increasing artificial reservoirs and aquaculture ponds in North China Plain. *Journal of Hydrology*, *608*, 127637. https://doi.org/10.1016/j.jhydrol.2022.127637

Zhu, X., Shi, P., & Pan, Y. (2012). Development of a gridded dataset of annual irrigation water withdrawal in China. In *2012 First International Conference on Agro- Geoinformatics (Agro-Geoinformatics)* (pp. 1–6). Shanghai, China: IEEE. https://doi.org/10.1109/Agro-Geoinformatics.2012.6311667

Table 1. Description of all experiments

Figure 4. (a) Annual precipitation (mm/day) and basic geostatic variables applied in this project including (b) topography (m), (c) cropland fraction (%), (d) irrigated land fraction (%), (e) groundwater dependence (%).

Figure 5. The relationship between FVEG and LAI+SAI in the NCP region. Thick solid line presents the original empirical relationship (Equation 1), fine solid line for best-fit relationship, while thick dash line for the adjusted equation (Equation 2).

Figure 6. Spatial distribution of (a) the cropping system, (b-e) harvest date and planting date for wheat and maize over a year based on the chronological order.

Figure 4. Spatial maps of (a) irrigation fraction (same as Figure 1d), (b) agricultural usage, (c) estimated irrigation usage, (d) statistical irrigation, e) satellite irrigation, f) observation irrigation, (g-i) simulated irrigation, and (j) MAD threshold adopted in IRRnew and GWnew.

Figure 5. Monthly irrigation (lines) and LAI (bars) from IRRdef, IRRnew and GWnew. Only crop grids in the NCP are counted.

Figure 6. Validation of the crop stage identification by comparing the wheat heading date, wheat maturity date, maize heading date, maize maturity date between the simulations and the observation

Figure 7. Validation of the annual cycle of leaf mass and stem mass at (a, c) Yucheng Station and (b, d) Shenyang Station. Dots represent station observation and lines are the simulation results.

Figure 8. Validation of crop yield of wheat and maize.

Figure 9. Monthly LAI pattern of the satellite observation, default crop model only, and after all modification and integration.

Figure 10. How models are connected. Red arrows are new connections added in this study.

Supplementary

Table S1. Parameter setting for spring maize and summer maize.

	Same as the parameter for one-year corn from Liu et al. (2016)
	Same as the parameter for one-year corn from Z. Zhang et al. (2020)
	Same as the parameter for spring wheat from Z. Zhang et al. (2023)
	Based on winter wheat study from Y. Zhang et al. (1991)
	Recalibrated with the station/satellite data

Parameter	Maize		Wheat	Physical meaning
	Spring	Summer	Winter	
GDDTBASE	10		0	Base temperature for GDD accumulation
GDDTCUT	30		30	Upper temperature for GDD accumulation
GDDS1	50		150	GDD from seeding to emergence
GDDS2	625		790	GDD from seeding to initial vegetative
GDDS3	1000		1190	GDD from seeding to post vegetative
GDDS4	1103		1600	GDD from seeding to initial reproductive
GDDS5	1555		2010	GDD from seeding to physical maturity
C3PSN	0		1	Indicator for C3 plant (1) or C4 plant (0)
KC25	30		30	CO_2 Michaelis-Menten constant at 25 °C
AKC	2.1		2.1	Q10* base for KC25
KO25	3.E4		3.E4	CO_2 Michaelis-Menten constant at 25 °C
AKO	1.2		1.2	Q10* base for KO25
AVCMX	2.4		1.5	Q10* base for VCMX25
VCMX25	60		80	Maximum rate of carboxylation at 25 °C
BP	4.E3		1.E4	Minimum leaf conductance
MP	4		9	Slope of conductance-to-photosynthesis
QE25 (1)	0.08		0.12	Quantum efficiency at 25 °C
Q10MR	2.0		2.0	Q10* base for maintenance respiration
LEFREEZ	268		268	characteristic T for leaf freezing
DILE_FC_S5	0.5		0.5	Coefficient for temperature leaf stress death
DILE_FC_S6	0.5		0.5	
DILE_FW_S5	0.2		0.2	Coefficient for water leaf stress death
DILE_FW_S6	0.2		0.2	
FRA_GR	0.2		0.2	Fraction of growth respiration
LF_OVRC_S5	0.2		0.05	Fraction of leaf turnover
LF_OVRC_S6	0.3		0.05	
ST_OVRC_S5	0.12		0.05	Fraction of stem turnover
ST_OVRC_S6	0.06		0.05	
RT_OVRC_S5	0.12		0.12	Fraction of root turnover
RT_OVRC_S6	0.06		0.06	

LFMR25	0.8		0.8	Leaf maintenance respiration at 25 °C
STMR25	0.05		0	Stem maintenance respiration at 25 °C
RTMR25	0.05		0	Root maintenance respiration at 25 °C
LFPT_S3	0.36	0.4	0.45	Fraction of carbohydrate flux to leaf
LFPT_S4	0.2	0.3	0.55	
LFPT_S5	0.1		0	
LFPT_S6	0.1		0	
STPT_S3	0.24	0.2	0.4	Fraction of carbohydrate flux to stem
STPT_S4	0.5	0.2	0.45	
STPT_S5	0.4	0.3	0.4	
STPT_S6	0	0.2	0.3	
RTPT_S3	0.4	0.3	0.15	Fraction of carbohydrate flux to root
RTPT_S4	0.3	0.5	0.0	
RTPT_S5	0.2	0.2	0.1	
RTPT_S6	0.1	0	0.1	
GRAINPT_S5	0.4	0.4	0.5	Fraction of carbohydrate flux to grain
GRAINPT_S6	0.8	0.7	0.6	
LFCT_S6 (2)	0		0.0005	Carbohydrate translocation from leaf to grain
STCT_S6 (2)	0		0.001	Carbohydrate translocation from stem to grain
BIO2LAI (3)	0.023	0.020	0.008	Leaf area per living leaf biomass

*Q10 means the rate increases by a 10°C temperature increases

(1) The QE25 parameter is increased following the removal of the great-overestimated and non-water-sensitive assumption 'FVEG=0.95'. This removal significantly decreases the radiation intercepted by vegetation, consequently imposing light limitations when calculating the photosynthesis. Since the crop model adopts the same photosynthesis function with other non-crop vegetation in the Noah-MP, for simplicity, we opt to raise the crop quantum efficiency to achieve higher photosynthesis without affecting other vegetation types.

(2) Carbohydrate translocation from leaf and stem to grain, which typically occurs during the reproductive stages, has been sometimes overlooked. However, we found it is necessary to include it when predicting the wheat yield in the highly productive NCP (X. Huang et al., 2020; Ma et al., 2006).

(3) The average station BIO2LAI is calculated to be 0.02 for maize and 0.01 for winter wheat approximately. However, the BIO2LAI varies a lot during different stages and different quadrats, which requires slightly recalibration around that station value. The final 0.023 for spring maize is similar to the 0.025 calibrated by (Yu et al., 2022) in the northeast China.

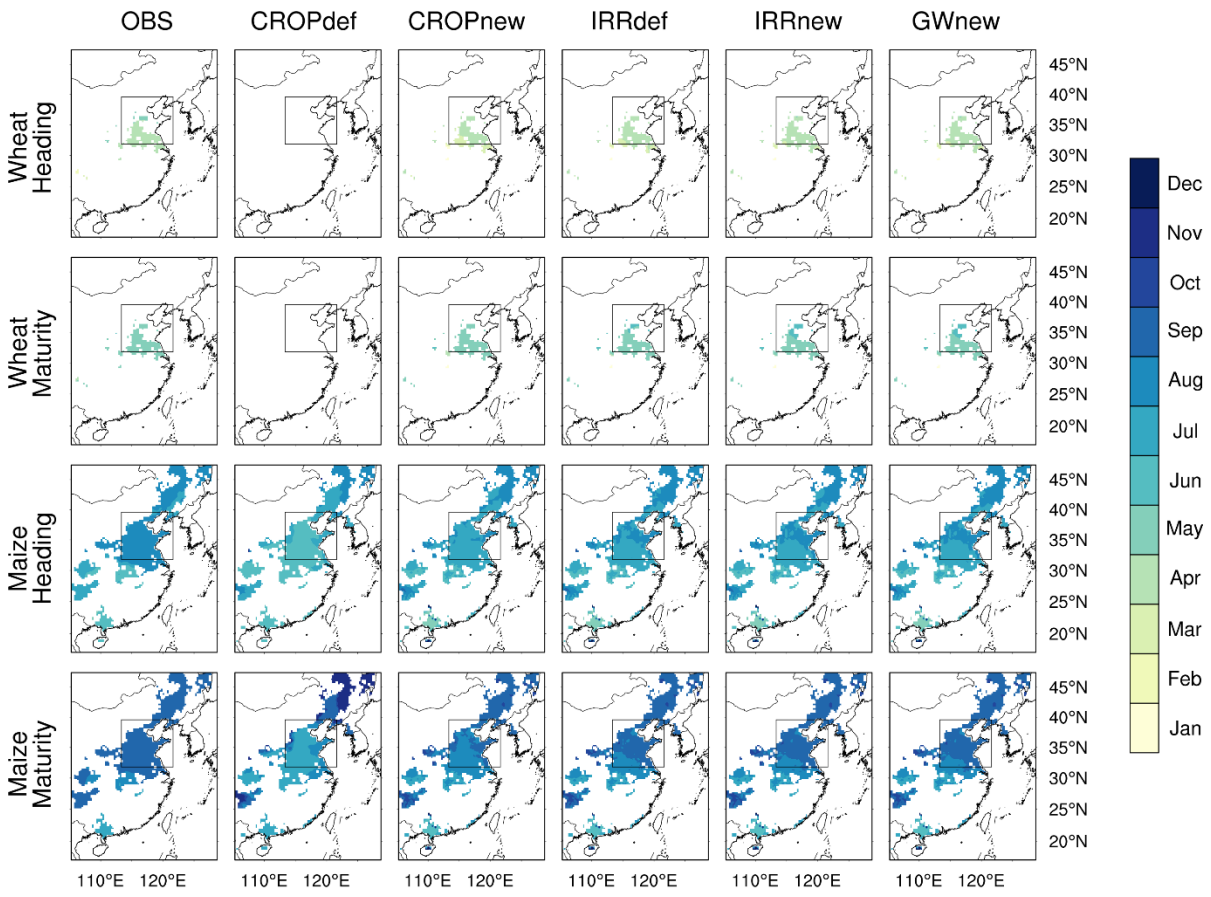

Figure S1. Validation of the crop stage identification by comparing the wheat heading date, wheat maturity date, maize heading date, maize maturity date between the simulations and the observation. This is an extended version of Figure 6.

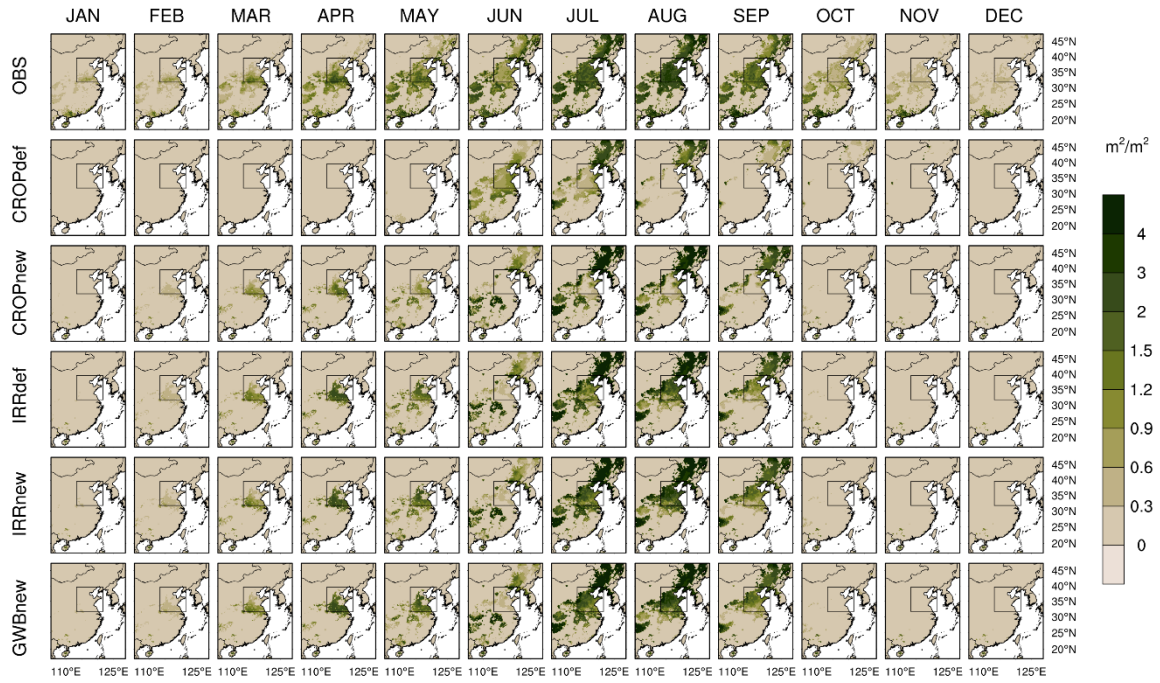

Figure S2. Monthly LAI pattern of the satellite observation, default crop model only, and after all modification and integration. This is an extended version of Figure 9.

Figure S3. Similar to Figure S2 but for FVEG. Notice that in the default crop model (CROPdef) all FVEG is fixed to 95%.